Superior performance as cathode material for intermediate temperature solid oxide fuel cells of the Ruddlesden–Popper n = 2 member $Eu_2SrCo_{0.50}Fe_{1.50}O_{7-\delta}$ with low cobalt content

Daniel Muñoz Gil,[a*] Khalid Boulahya,[b] María Santamaria Santoyo,[b] M.Teresa Azcondo[c] and Ulises Amador[c]

[a] Instituto de Cerámica y Vidrio, CSIC, Cantoblanco, 28049 Madrid, Spain

[b] Departamento de Química Inorgánica, Facultad Ciencias Químicas, Universidad Complutense, E-28040 Madrid, Spain.

[c] Universidad San Pablo-CEU, CEU Universities, Facultad de Farmacia, Departamento de Química y Bioquímica, Urbanización Montepríncipe, Boadilla del Monte, E-28668, Madrid, Spain

Abstract

The effects of the contents of iron and cobalt on the crystal structure, oxygen content, thermal expansion coefficient and electrical-electrochemical properties of materials $Eu_2SrCo_xFe_{2-x}O_{7-\delta}$ (x= 0.50 and 1.00) are reported. These oxides are well-ordered new members of the Ruddlesden–Popper series $(Eu,Sr)_{n+1}(Co,Fe)_nO_{3n+1}$ system with n=2 as determined by selected area electron diffraction and high-resolution transmission electron microscopy and X-ray diffraction studies. The two materials are semiconductors of p-type, with much higher total conductivity under working conditions for the low-cobalt compound, $Eu_2SrCo_{0.50}Fe_{1.50}O_{7-\delta}$. Composites cathodes prepared with this oxide present much lower area-specific resistance values (0.08 $\Omega \cdot cm^2$ at 973 K in air) than composites containing

$Eu_2SrCo_{1.00}Fe_{1.00}O_{7-\delta}$ (1.15 $\Omega \cdot cm^2$). This significant difference is related with the much higher total conductivity and a sufficiently high content of oxygen vacancies in the Fe-rich phase. The excellent electrochemical performance of $Eu_2SrCo_{0.50}Fe_{1.50}O_{7-\delta}$ with low cobalt content, which show one of the lowest area-specific resistance reported so far for a Ruddlesden–Popper oxide, makes it a good candidate for application as a cathode material for Solid Oxide Fuel Cell at intermediate temperature in real devices.

1. Introduction

In the search for cathode materials for intermediate temperature solid oxide fuel cells (IT-SOFC) oxides of the Ruddlesden–Popper (R–P) family are attracting much attention.[1-12] The Ruddlesden–Popper (R–P) series[13, 14] with the general formula $A_{n+1}M_nO_{3n+1}((AMO_3)_nAO)$ (A = rare-earth and/or alkaline-earth elements and M = transition metal with n=1, 2, etc), comprise a vast family of oxides. The structure is built up by perovskite blocks of n-octahedra layers which alternate with single AO rock salt layers (see Figure 1). Within the perovskite-like blocks, built up from corner-sharing MO_6 octahedra, electronic conduction may occur when M-cations at the center of the octahedra present multiple non-localized oxidation states. Anionic vacancies and/or interstitial oxygen ions may exist in the AO rock-salt layers, resulting in ionic conduction. The combination of these two properties make the R-P oxides mixed ionic-electronic conductors (MIEC), which are potentially useful as SOFC cathode component.

It is well established that SOFC cathode materials should enhance the reduction of molecular oxygen to oxygen anions (Oxygen Reduction Reaction, ORR); so, high catalytic activity is needed. Once formed, oxide ions must diffuse through the cathode to the electrolyte; thus, sufficiently high ionic conductivity is required.[15] In the ORR electrons also participate, hence

cathode material with high electronic conductivity are preferred to minimize ohmic losses. As a guide, electrical conductivity under operating conditions, greater than 100 $S \cdot cm^{-1}$ is desirable.[16] It is evident that mixed ionic-electronic conductors are the best candidates for air electrodes in SOFCs.

To develop real devices using low-cost materials for structural components and interconnectors, and to improve cell duration, the SOFC operating temperature must be lowering down to 1073 K (the so-called intermediate temperatures in the range 773–973 K). This is a challenging objective since the cell resistance may noticeably increase at low temperature. In particular, the cathode performances strongly depend on temperature since mixed conduction as well as catalytic activity may be unacceptable low in the intermediate temperature (IT) range. As a reference, it is accepted that for practical applications the cathode should have a specific-area resistance (ASR, the observed resistance due to all the processes occurring at the electrode) lower than 0.15 $\Omega \cdot cm^2$ at working temperature.[17] Several materials reach this value at sufficiently high temperature.[18-23] However, the design and preparation of cathode materials showing high performance at moderate temperatures is still a pending objective for the development of IT-SOFCs.

Cobalt-based oxides (in particular with perovskite structure) have been intensively investigated since they display good MIEC properties and high activity for ORR.[24-29] However, cobaltites usually present serious drawbacks due to structural instability, chemical reaction and mechanical incompatibility with other SOFC components (in particular with the electrolyte).[30] Mechanical incompatibility is due to the large thermal expansion coefficient (TEC) of cobalt oxides, much larger than those of commonly used electrolytes $Ce_{0.8}Gd_{0.2}O_{2-}$

δ (CGO) at intermediate temperature and yttria-stabilized zirconia (YSZ) at high temperature, often due to spin transitions of cobalt ions.[31-34]

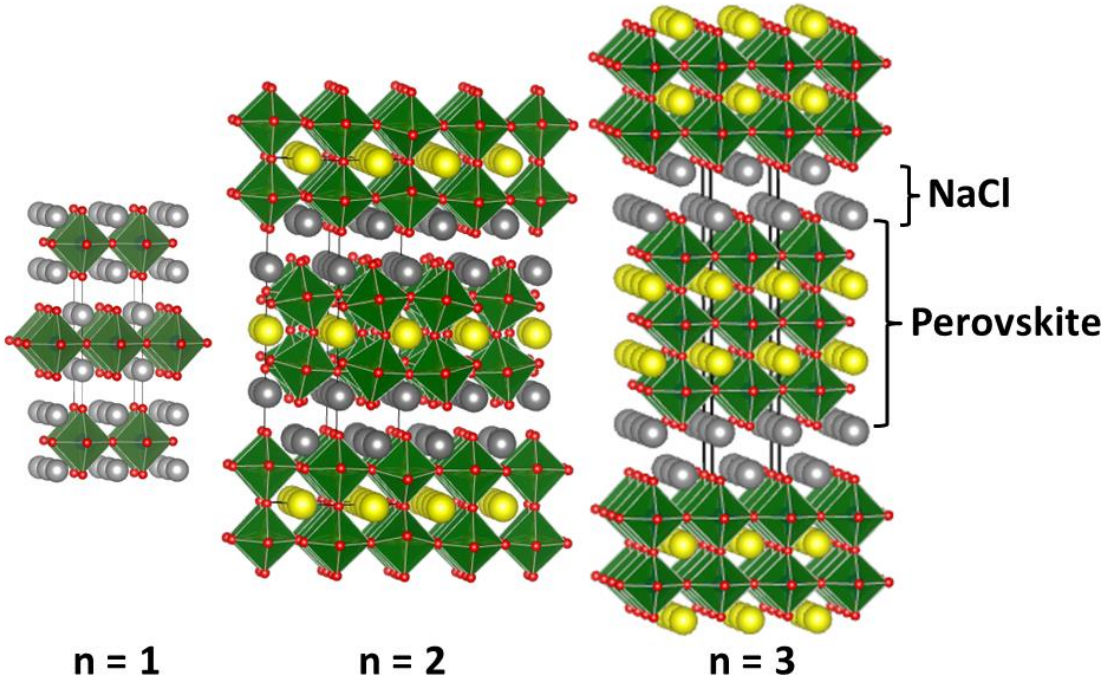

Figure 1. Drawings of the structures of the Ruddlesden–Popper series with n = 1, 2 and 3, consisting of perovskite-like blocks of n layers separated by a NaCl-like sheet.

Among the R–P series many oxides with n=1 have been studied as air-electrode in SOFC[2, 8, 11, 12] and some of them display noticeable performances as air-electrode of IT-SOFCs.[1, 3, 9-11] However, only few articles reporting the properties of n=2 and 3 members have been publisehd.[4, 5, 7, 35-41] More recently some R-P oxides with n=2 have been reported as good materials for cathodes of protonic ceramic fuel cells (PCFC).[42-44]

In previous papers we reported the properties of Co-containing n=2 R-P oxides, that have good catalytic activity for ORR and high electronic conductivity; however their show relatively high thermal expansion coefficients (TEC).[5, 7] Substitution of Co by other 3d-metal decreases TEC; a concomitant detrimental effect on the electronic conductivity induces the increase of ASR.[2, 7, 45-47] In particular, for the oxide $Eu_2SrCo_{1.50}Fe_{0.50}O_{7-\delta}$ we reported a low ASR value of 0.26 $\Omega \cdot cm^2$ at 973 K in air. As a continuation of our studies on the $Eu_2SrCo_xFe_{2-x}O_{7-\delta}$ n=2 R-P series,[7] in the present paper compounds with lower cobalt-contents, x=1.00 and 0.50, has been prepared and studied with the aim of lowering the TEC and explore the effect of higher iron-contents on the electrochemical properties. X-ray diffraction and electron microscopy were used for structural characterization. Their suitability as cathode components in IT-SOFCs were explored; comprising the electrical and electrochemical properties, as well as the mechanical and chemical compatibility with CGO.

2. Experimental

Polycrystalline samples of composition $Eu_2SrCo_xFe_{2-x}O_{7-\delta}$ (x=0.50 and 1.00, ESCF0515 and ESCF1010) were synthesized by modified Pechini method involving several steps and with final thermal treatments different for the two samples. To obtain 2 grams of material, in the first step stoichiometric amounts of $Co(NO_3)_2 \cdot 6H_2O$ (Aldrich, 99.90%), $Eu(NO_3)_3 \cdot 5H_2O$, $Sr(NO_3)_2$ (Aldrich 99.0%) and $Fe(NO_3)_3 \cdot 9H_2O$ (Aldrich 99.95%), were dissolved in 50 ml of distillate water. Keeping heating and stirring, citric acid was added in an acid-to-metal-ions ratio 3:1. When the solution volume is reduced to a half of its initial volume, 3 ml of diethylene glycol was added to initiate polymerization. After few minutes a solid resin is formed; then it is cooled down to room temperature and ground in an agate mortar. The obtained powder was fired at 1173 K overnight to remove organic matter. The powders

obtained after milling and homogenization were submitted to different treatments in air depending on the Co/Fe ratio. The sample ESCF1010 was heated at 1573 K for four days and then quenched to room temperature. On the other hand, ESCF0515 was obtained heating the precursor at 1473 K for four days and cooling down to room temperature by turning off the furnace.

Samples purity was determined by powder X-ray diffraction (PXRD) on a Bruker D8 high-resolution diffractometer equipped with a LynxEye® fast detector using monochromatic $CuK_{\alpha 1}$ (λ = 1.5406 Å) radiation obtained with a germanium primary monochromator. X-ray diffraction patterns of enough quality and resolution for structural refinement were obtained adjusting the angular range, step size and counting times. Diffraction data were analyzed using the Fullprof software;[48] peak shape was described by a pseudo-Voigt function, and the background level was fitted with linear interpolation. . In addition, to evaluate the stability of ESCF1010, which was prepared by quenching from high temperature, a small amount of the material was heated at 1073 K for several days (14 days) and subsequently it was slowly cooled down to room temperature.

The average oxidation state of 3d-ions (Co and Fe) and oxygen content (assuming charge neutrality) of samples were determined by redox titration as described in a previous paper[49] and Thermogravimetric Analysis (TGA) on a Netzsch 409PC apparatus; after an isothermal step at 423 K to remove species adsorbed on the solid surface, heating and cooling steps in air at 10 $K \cdot min^{-1}$ between that temperature and 1273 K are performed. The amount of each sample used for TGA experiments is about of 400 mg. Information on oxygen stoichiometry and materials stability from RT to working conditions (up to 1173 K) is also obtained from TGA data.

Selected area electron diffraction (SAED) and high-resolution transmission electron microscopy (HRTEM) studies have been performed on a JEOL JEM 3000F microscope operating at 300 kV (double tilt (±20º) (point resolution 1.7Å)), fitted with an energy-dispersive X-ray spectroscopy (XEDS) microanalysis system (OXFORD INCA). For these Transmission electron-microscopy experiments were performed on finely ground materials using n-butyl alcohol as grinding media and ultrasonically dispersed. A few drops of the resulting suspension were deposited in a carbon-coated grid.

A TM-1000 Hitachi scanning electron microscope (SEM) was used to determine the electrodes microstructure, porosity and adhesion on the electrolyte support, before and after the impedance measurements.

Bars with dimensions around 11x4x4 mm^3 were prepared for d.c. and dilatometry measurements by sintering the corresponding amount of powder (about 1 g) at 1473 K for 2 h. The purity of the samples after the conformation of the bars, as well as after the corresponding measurements (either d.c. or dilatometry) was confirmed by PXRD; the relative densities of the bars was determined by the Archimedes method.

Total electrical conductivity was determined by d.c. four-probe measurements on rectangular dense bars using a potentiostat/galvanostat apparatus working in galvanostatic mode (Autolab PGSTAT302N). Experiments were performed in air, O_2 and N_2 atmospheres. The resistances of the samples were obtained in the temperature range of 423–1223 K from the slopes of the linear I–V plots. Every conductivity dataset was obtained after the sample was stabilized at 1223 K for 12 h in a given atmosphere, then the measurements were performed from this temperature to 473 K (cooling rate of 5 K min^{-1}) every 50 K after stabilization for 15 min.

Chemical compatibility of ESCF1010 and ESCF0515 with the CGO was proven prior to the electrochemical studies: sample+CGO mixtures (70:30 wt %) were heated at 1173 K for 12 hours and further analyzed by PXRD

The electrochemical properties of the $Eu_2SrCo_xFe_{2-x}O_{7-\delta}$ (x=0.50 and 1.00) oxides as a cathode in IT-SOFCs with CGO electrolyte were studied by impedance spectroscopy (IS) in air in the temperature range 773–1173 K. Impedance spectroscopy was performed using a symmetrical two-electrode configuration cells. Electrode materials ($Eu_2SrCo_xFe_{2-x}O_{7-\delta}$:CGO composites, 70:30 wt%) were mixed with a binder (Decoflux™, WB41, Zschimmer and Schwartz), deposited, with a brush on opposite sides of CGO electrolyte pellets and cured at 1173 K for 3 h. Highly densified cylindrical pellets of the electrolyte $Ce_{0.9}Gd_{0.1}O_{2-\delta}$ (CGO, Rhodia), with relative density > 98% and dimensions 10 mm diameter and 1.2 mm thickness, were obtained by sintering green pellets prepared, at RT by uniaxial pressing (5 Tm cm^{-2}), at 1673 K for 10 h. Platinum paste was used as current collectors on both sides of the pellets, once deposited the collectors were cured 1223 K for 1 hour. Impedance spectroscopy measurements were conducted using an Autolab PGSTAT302 N instrument equipped with a FRA2 module; a signal amplitude of 50 mV was applied, and the spectra were obtained in the frequency range 0.1–10^6 Hz. The impedance spectra were fitted to circuital models using the Zview software.[50] The ASR values have been determined from the resistance obtained by extracting the contributions from the electrolyte and the measuring-device, normalized by the electrode area and divided by 2, which is common practice using symmetrical cells.[15, 51]

Dilatometry was carried out to determine the materials TECs on rectangular bars using an Adamel Lhomargy DI-24 thermomechanical equipment in the temperature range 298–1173 K with a heating rate of 5 $K \cdot min^{-1}$.

3. Results and Discussion

3.1. Structural Characterization

The procedures to obtain $Eu_2SrCo_{1.00}Fe_{1.00}O_{7-\delta}$ and $Eu_2SrCo_{0.50}Fe_{1.50}O_{7-\delta}$ are noticeable different. To prepare pure ESCF1010 samples somewhat higher temperature is needed and, more importantly, the sample must be quenched from the (high) synthesis temperature to RT. Other members of the series $Eu_2SrCo_xFe_{2-x}O_{7-\delta}$ ($x \geq 1.5$) or other R-P analogous, with high cobalt contents display a similar behavior, as previously reported.[5, 7]

On the contrary, the samples of ESCF0515 are prepared at lower temperature and slowly cooled to RT. This is the main difference related with low cobalt (high iron) contents. It seems that the 3d-metal oxidation state is close to +3 in the R-P n=2 compounds;[7, 52] since cobalt is much prone than iron to reach oxidation states higher than three, the compositions with high cobalt-contents must be quenched from temperatures sufficiently high to ensure a pO_2 in air low enough and to avoid its oxidation when slowly cooled, and the consequent formation of impurities with cobalt in higher oxidation state such as $SrCoO_{3-d}$.[53] The situation is totally different for material with high contents of iron; in these cases slow cooling ensures that iron reaches the trivalent state needed to stabilize the structure, as observed in $SrEu_2Fe_2O_{7-\delta}$, the end member of the studied $Eu_2SrCo_xFe_{2-x}O_{7-\delta}$ series.[52]

Samples of both compounds of nominal compositions $Eu_2SrCo_xFe_{2-x}O_{7-\delta}$ ($x = 0.50$ and 1.00) were obtained as single-phase sample as confirmed by PXRD. All the Bragg maxima in the patterns are indexed with tetragonal unit cells: $a = 5.40$ Å and $c = 19.55$ Å. The reflection

conditions ((*0kl) k+l=2n, (0k0) k=2n and (00l) l=2n)*) suggest as possible Space Groups (S.G.): $P4_2nm$ (#102), P-4n2 (#118) or $P4_2/mnm$ (#136). This latter S.G. corresponds to the symmetry of $Eu_2SrFe_2O_{7-\delta}$ oxide.[52, 54, 55]

This tetragonal symmetry is confirmed by SAED patterns and HRTEM micrographs along different zone axes, used to reconstruct the reciprocal and real space lattices for the two phases $Eu_2SrCo_xFe_{2-x}O_{7-\delta}$ (x = 0.50 and 1.00). Both oxides are isostructural, in agreement with PXRD results; they are also isostructural with the x=1.5 member of the family previously reported[7] and with the endmember x = 0.[52] Insets in Figure 2a and 2b show the SAED patterns along the [010] zone axe, where all reflections can be indexed in the primitive tetragonal lattice determined by PXRD (a=5.40 Å and c=19.55 Å). In addition, the extinction conditions confirm the possible S.G. deduced by PXRD. The contrast differences of the HRTEM images of both phases along the [010] zone axis (Figure 2) reveal an apparently well-ordered material with d-spacing of 3.8 Å and 19.5 Å, corresponding to d_{110} and d_{001}. The contrast along the c-axis observed in these images consists of two adjacent bright dots shift by ½ d_{110} that can correspond to the Eu atoms in the rock-salt block. The perovskite blocks (that consist of $(Co/Fe)O_6$ octahedra and Sr ions) are observed as dark contrast zones (the octahedra) with slightly brilliant dots ascribed to Sr ions. A sketch of the structure model is included in Figures 2a and 2b. Such contrast variation is characteristic of n=2 member of Ruddlesden–Popper series, as previously reported.[7, 54, 55] As can be seen in both Fourier transforms of the HRTEM images, there are no signs of microdomains or extra spots that may suggest an additional order. Therefore, ESCF1010 and ESCF0515 compounds present a well-ordered structure of the n = 2 member of the Ruddlesden–Popper series (Figure 1), at both local and average scale (as discussed in what follows).

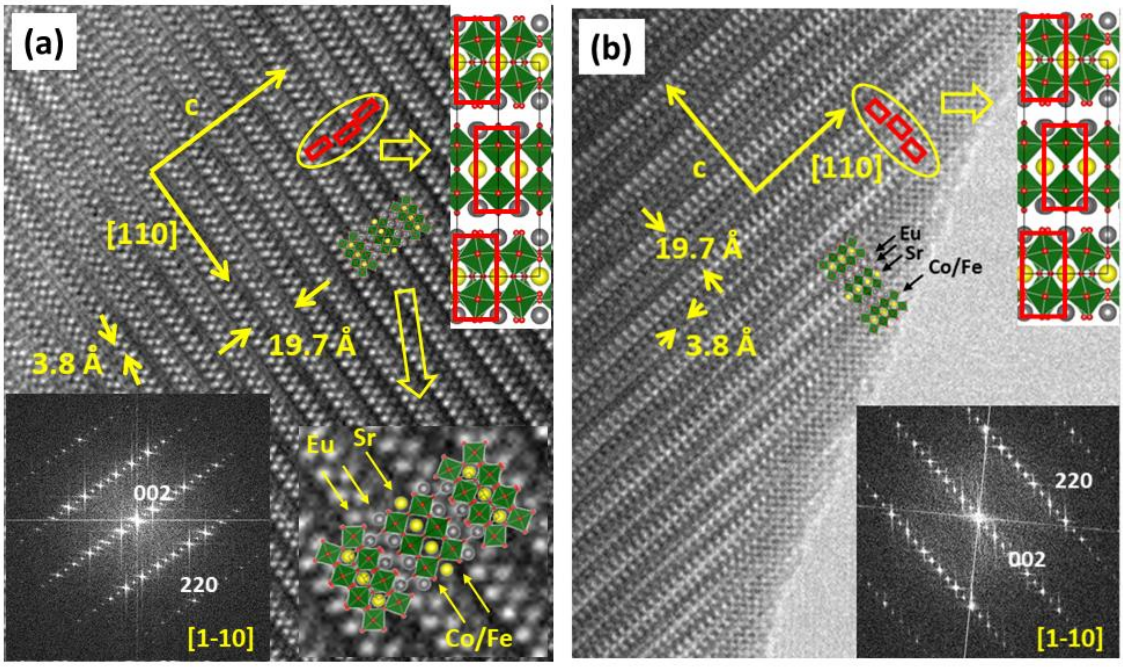

Figure 2. HRTEM images taken along the [1-10] zone axis of (a) $Eu_2SrCo_{1.00}Fe_{1.00}O_{7-\delta}$ and (b) $Eu_2SrCo_{0.50}Fe_{1.50}O_{7-\delta}$. Optical Fourier transform (FT) are shown as insets. Schematic representations of the structure along the [1-10] direction are included.

Using the above results and our previous ones on similar systems,[5, 7] a structural model is proposed for the two materials under study, based on the structure of a n = 2 member of the R-P series with symmetry $P4_2/mnm$.[52] The fit of the PXRD data to the model, given in Table S1, confirms its validity to describe the average structure of the title compounds. At this point it must be commented that neutron powder diffraction, which is a technique suited to deal with those structural features related to the oxygen substructure, cannot be used in this case due to high neutron absorption of Co and Eu, that preclude to obtain any conclusive result, as experienced in a previous work.[7]

Ordering of Sr^{2+} and Ln^{3+} ions occurs in similar R-P oxides $Sr_{2-x}Ln_xMn_2O_7$ in the two A-cations sites. The large Sr^{2+} ions prefer the A-sites in the perovskite blocks, whereas smaller

lanthanides ions mainly occupy the A-site in the rock-salt layers.[56] The distribution of Eu/Sr over the two crystallographic A-sites was refined; total cationic ordering was obtained in both materials. Cobalt and iron cations seem to be randomly distributed over the octahedral sites in the B sublattice since no evidences of order were detected by none of the structural techniques. To limit the number of refined parameters and to ensure the convergence of the refinements, a Debye-Waller factors for each kind of atom was used (same for all the oxygens). It was possible to refine the positions and occupancies of all atoms; since Fe and Co are indistinguishable by PXRD, theirs contents were assumed as the nominal ones. Full populations of all sites, within the experimental error, (including oxygen atoms) are obtained. Figures S1a and S1b show the graphic results of the fitting of the experimental X-ray diffraction patterns and the difference between observed and calculated data.

Neither vacancies in the anion substructure, nor interstitial oxygen atoms are observed in the rock-salt layer, in agreement with the oxygen content determined by chemical titration for the two compounds. The combination of these techniques confirms an oxygen content close to the nominal one with no extra oxygen. For the oxides $Eu_2SrCo_xFe_{2-x}O_{7-\delta}$ the average oxidation states of 3d-metals are determined, by titration, to be 3.00(2) and 2.97(2) for x = 0.50 and 1.00, respectively. Assuming electroneutrality, the corresponding oxygen content of the as-prepared samples are 7.00(2) and 6.97(2).

The final refined structural parameters are presented in Table S1, whereas Table S2 shows some selected interatomic distances. The structure refinements confirm that both materials are isostructural with $Eu_2SrFe_2O_7$[52] in agreement with the HRTEM results. Figure 3 depicts a schematic representation of the structure.

A remarkable unit cell expansion is observed as the iron content increases along the whole $Eu_2SrCo_xFe_{2-x}O_{7-\delta}$, with unit cell volume ranging from 568.65(3) $Å^3$ for x=1.50[7] to 588.40(3) $Å^3$ for x = 0.50 and 597.72(2) $Å^3$ for x = 0.[52] This large cell expansion strongly suggests that high-spin Fe^{3+} ions replace low-spin trivalent cobalt ions. A simple geometrical consideration based on ionic radii, ($^{VI}r(Fe^{3+})^{HS}$ = 0.645 Å, $^{VI}r(Fe^{3+})^{LS}$ = 0.55 Å, $^{VI}r(Co^{3+})^{HS}$ = 0.61 Å and $^{VI}r(Co^{3+})^{LS}$ = 0.545 Å),[57] shows that only this scheme can account for the large unit cell variation upon substitution. Besides, in many cobaltites trivalent cobalt is in LS state at RT, being the LS → HS transition responsible for the large TECs they present,[31, 33, 34] in such a way the larger the Co^{3+} content the bigger the TEC.

As in other n=2 R-P compounds, in the perovskite-like blocks (i.e. corner-sharing octahedra), the BO_6 octahedra are tilted with a Glazer[58] scheme ($a^-a^0c^0$) (block at the bottom of the unit cell) and ($a^0a^-c^0$) (block at the middle of the cell). Thus, out-of-phase tilt occurs along one of the pseudo-perovskite axes in every two-layer block, being the direction of tilting rotated by 90º from one block to the adjacent ones. Along the four-fold axis no tilt is produced. As the iron content increases, not only the B-O distance becomes larger, as expected from the ionic sizes given above, but the perovskite blocks are more distorted. This is what one expects based on the Goldschmidt tolerance factor that is closer to unity (value corresponding to a non-distorted cubic perovskite structure) for lower iron contents (Table S2).

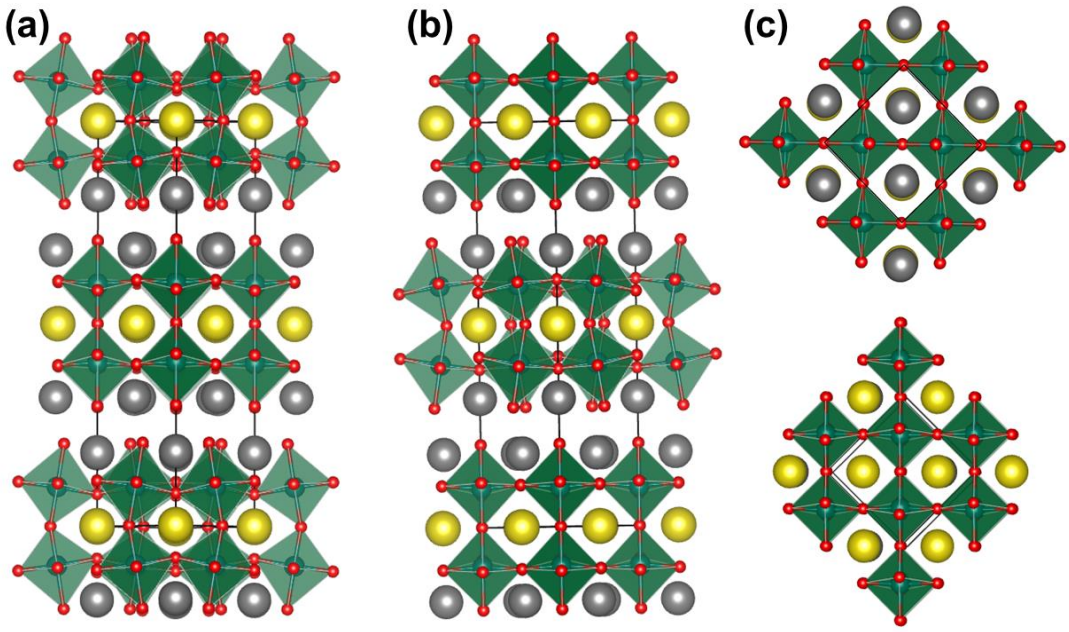

Figure 3. **(a)** Projection along the [110] direction of the structure of $Eu_2SrCo_xFe_{2-x}O_{7-\delta}$, **(b)** drawing along [1-10] and **(c)** view along the c-axis of the perovskite blocks. Co and Fe occupy the centers of green octahedra of oxygens (small red balls); Sr ions are represented as yellow balls, whereas the grey ones correspond to Eu.

3.2. Thermal stability and expansion. Compatibility with the electrolyte

The chemical stability (oxygen loss or gain) of the materials and the compatibility with the electrolyte (CGO), was studied in conditions like those used to process the electrodes and in electrochemical experiments. The thermal expansion coefficient (TEC) was evaluated, as well.

$Eu_2SrCo_{1.00}Fe_{1.00}O_{7-\delta}$ is prepared by quenching from high temperature (1573 K), existing as a metastable phase at lower temperatures. Hence, it is relevant to determine its stability in the IT-SOFC conditions. About 100 mg of the material was treated at 1073 K for two weeks and slowly cooled down to room temperature. No decomposition was observed after this treatment in by PXRD (pattern not shown). Therefore, once the n=2 R-P structure is formed,

the material remains as a metastable phase when treated at not very high temperature for a long period; even more, by heating the tittle oxides close to the synthesis temperatures for a short time (like the conditions used to prepare the bars for d.c. measurements: 1473 K for 6 hours) no decomposition is observed in the PXRD patterns (not shown).

Chemical compatibility of ESCF1010 and ESCF0515 with the electrolyte (CGO) was evaluated by heating blends of each sample with CGO (70:30 wt%) at 1173 K for 12 hours. The PXRD patterns in Figure S2 only present the Bragg maxima corresponding to the original components, suggesting that either the reaction between the blends components does not occur, or the amount of new phase(s) is below the detection limit of PXRD.

Relative linear thermal expansion was measured on dense (relative densities greater than 95%) sintered bars of both samples, $Eu_2SrCo_xFe_{2-x}O_{7-\delta}$, (x= 0.50 and 1.00). Before and after the experiment the phase composition of the bars was determined by PRXD; no decomposition of the R-P n=2 phases, ESCF1010 and ESCF0515, is observed. The results are presented in Figure S3 for the range 300–1273 K; the TEC is obtained from the slope of these plots. It is evident that the slope is not constant in the entire temperature range. Two almost linear regimes are observed, one at low temperature, 300-600 K, with similar slopes (TECs) for both samples and another with a steeper slope at high temperature (900-1073 K) and noticeably different for the two compounds. Usually, high TECs of cobaltites are related to spin transitions of HS-Co^{3+}; however, the rise of TEC associated with thermally activated oxygen release is well known in Co- and Fe-based systems.[59,60] In the present case, both oxides lose oxygen from relatively low temperatures (Figures S3b and S4). As the Fe-content increases in the $Eu_2SrCo_xFe_{2-x}O_{7-\delta}$ series, the TEC values (for the whole temperature range in Figures S3a) decreases from 19.15×10^{-6} K^{-1} for x=1.00 to 16.57×10^{-6} K^{-1} for x=0.50. Large

TECs are usually associated with high oxygen losses, but in the present oxides the differences of TECs values are most likely due to the lower concentration of Co^{3+} for x = 0.50 that limits the effect associated with spin-state transitions commonly observed in cobaltites.[45, 59, 61]

3.3. Electrical conductivity

Four-probe d.c. electrical measurements were performed on dense (relative densities greater than 92%) sintered bars of the samples under study. Before and after the experiment the phase composition of the bars was determined by PRXD; no decomposition of the materials is observed. The measurements were carried out three times on different bars; Figure 4 displays representative values of the electrical conductivity of the compounds $Eu_2SrCo_xFe_{2-x}O_{7-\delta}$ (x=0.50 and 1.00) as a function of temperature in different atmospheres; the data for x=1.5 in air (taken from ref. [7]) are also included for comparison. Total conductivity (electronic plus ionic) for ESCF1010 and ESCF0515 increases on heating in the whole temperature range despite the ambient pO_2, revealing a semiconductor-like behavior. In the entire temperature range, conductivity increases with the oxidizing character of the gas, which indicates *p-type* electronic conduction due to holes-hopping associated to 3d-ions in mixed oxidation states; i.e. hole transfer between $(Co,Fe)^{3+}$ and $(Co,Fe)^{2+}$ sites.

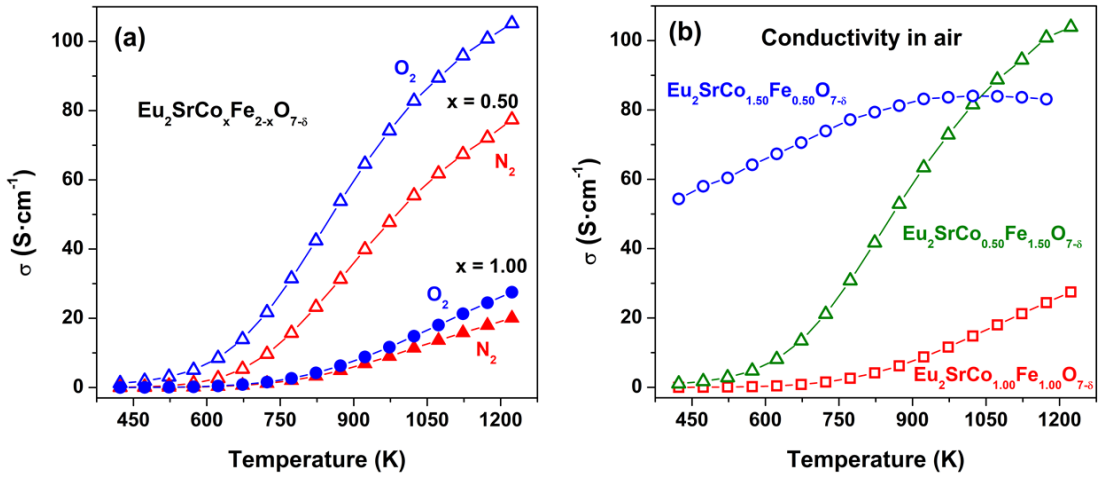

Figure 4. (a) Electrical conductivity as a function of temperature for $Eu_2SrCo_xFe_{2-x}O_{7-\delta}$ (x=0.50 and 1.00) in O_2 and N_2, (b) Electrical conductivity as a function of temperature in air for ESCF1010 (red line), ESCF0515 (green line) and ESCF1505 (blue line, data from Boulahya, K.et al. *J. Mater. Chem. A* **2019,** 7, 5601-5611).

Under N_2 conductivity remains very low and almost identical for both samples up to 600 K; at higher temperatures ESCF0515 shows higher conductivity than ESCF1010. In the low temperature range *p-type* carries (holes) are annihilated: oxygen loss occurs in a significant extent producing *n*-type charge accordingly to Eq. (1) that annihilates *p-type* carriers Eq. (2):

$$O_O^x \rightleftarrows \tfrac{1}{2}\,O_2 + V_O^{\bullet\bullet} + 2\,e' \qquad (1)$$

$$h^{\bullet} + e' = \text{null} \qquad (2)$$

In a localized formalism, electrons are trapped by Co^{3+} and/or Fe^{3+} that are reduced to divalent state:

$$Co_{Co}^x \rightleftarrows Co_{Co}' + h^{\bullet} \qquad (3)$$

$$Fe_{Fe}^x \rightleftarrows Fe_{Fe}' + h^{\bullet} \qquad (4)$$

$$O_O^x + 2\,h^\bullet \rightleftarrows V_O^{\bullet\bullet} + \tfrac{1}{2}\,O_2 \qquad (5)$$

Although the redox pair Eu^{3+}/Eu^{2+} plays a role in the electrical and electrochemical properties of some oxides,[62] reduction of Eu^{3+} only occurs under strongly reducing conditions (pO_2 below 10^{-22} atm) well below the values used in the experiments presented in this paper.

It is well known that in mixed hopping conductors, where there is more than one type of transition-metal cations, charge carriers tend to follow paths requiring the lowest energy. For example, in $SmBaCo_{2-x}Fe_xO_{5+\delta}$,[63] $Nd_{0.6}Sr_{0.4}Co_{1-y}Mn_yO_{3-\delta}$[64] and $GdBaCo_{2-x}Mn_xO_{5+\delta}$[61] systems, the Co sites have lower small-polaron site energy than the Fe or Mn sites. In low concentration high-energy sites will act as traps to temporarily immobilize the charge carriers. However, if their population increases enough, the carriers could move via these high-energy sites.[21, 65] Thermal evolution of total conductivity for oxides $Eu_2SrCo_xFe_{2-x}O_{7-\delta}$ (x = 0.50, 1.00 and 1.50) in air are shown in Figure 4b. The high-Co compound shows the highest conductivity from 150 K (47.1 $S\cdot cm^{-1}$) to 800 K (79.5 $S\cdot cm^{-1}$); at same temperatures the corresponding values for the other compositions are noticeably lower: for ESCF1010 (0.013 and 4.05 $S\cdot cm^{-1}$) and for ESCF0515 (1.04 and 41.7 $S\cdot cm^{-1}$). Since the Co sites possess lower small-polaron site energy than the Fe, total conductivity will increase with the Co^{3+}/Co^{2+} pair concentration. However, the high-Fe containing compound (ESCF0515) displays higher conductivity than ESCF1010. In this latter compound the content of Fe is high enough to significantly perturb the conduction paths with low energy, whereas in the former oxide there is enough content of Fe^{3+} for the movement of holes to take place through adjacent high-energy Fe sites. As expected, (and observed in Figure 4b) the activation energy for this mechanism is larger than that involving low-energy Co-sites. Thus, at high enough

temperature the conductivity of ESCF1010 becomes relatively high. Therefore, conduction is dominated polaron hopping between Fe^{3+} and Fe^{2+} sites. It is important to note that, in oxides, trivalent cobalt is more prone to be reduced than trivalent iron,[66] so the oxygen loss observed in TGA will induce a negligible decrease in the concentration of active charge carriers. Thus, the concentration of electronic conducting species, associated with Fe^{3+}/Fe^{2+} pairs, should be considerably nearly temperature-independent, in agreement with what observed for the material with higher iron content.

3.4. Polarization tests on symmetrical cells

Electrochemical characterization was performed by IS on symmetrical cells made of composites $Eu_2SrCo_xFe_{2-x}O_{7-\delta}$:CGO (70:30 w%) (x = 0.50 and 1.00) on CGO electrolyte pellets measured in temperature range 773-1123 K. The spectra were measured three times on different cells. Worth to note, the addition of electrolyte powder to form a composite is needed to get good adhesion of the electrode on the electrolyte.

Figures 5 displays the fits of the IS data corresponding to ESCF1010 to circuital models built as detailed in what follows.

The calculation of distribution of relaxation-times (DRT) is a powerful tool to identify the number and nature of the processes observed in the IS spectra, since it provides a high resolution function to discriminate the processes.[67] Thus, we computed DRT functions from the IS data. As examples, Figure 6 displays those corresponding to ESCF1010 at 873 K and 1073 K.

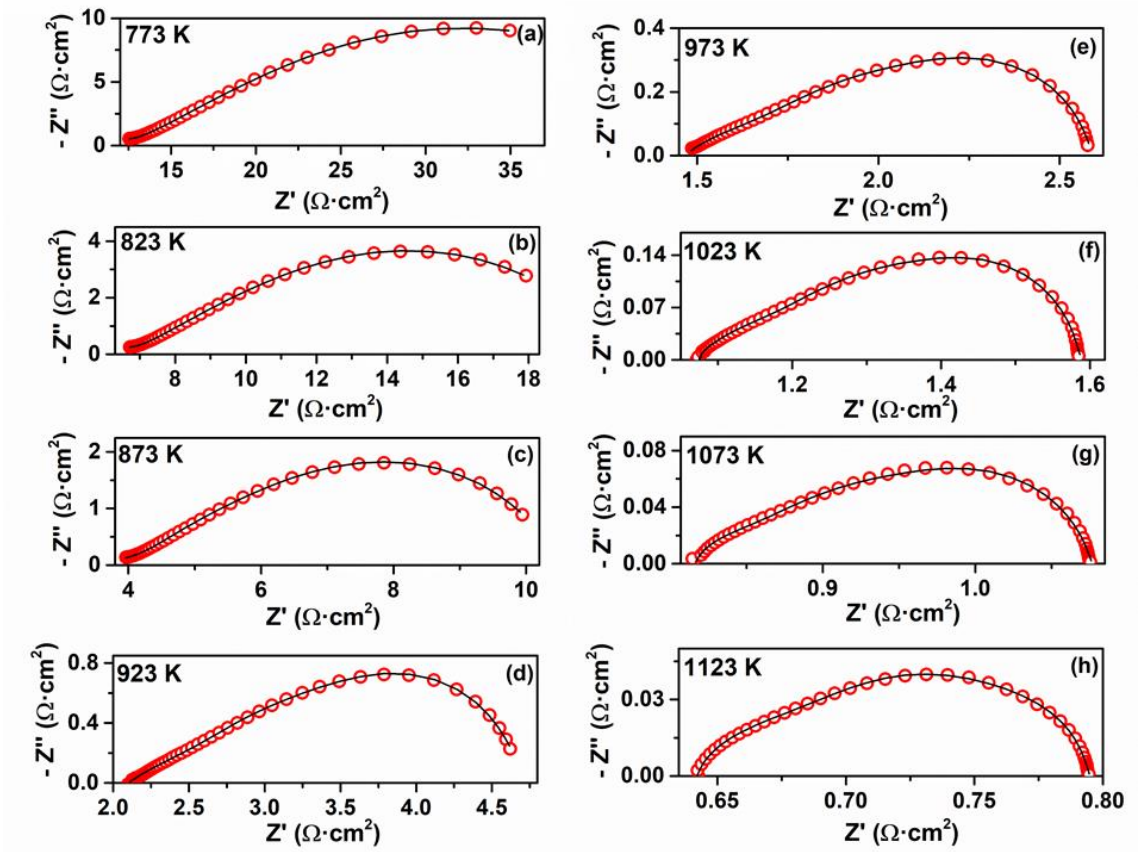

Figure 5. Impedance spectra at operation temperatures from 773 to 1123 K in air on symmetrical cells with $Eu_2SrCo_{1.00}Fe_{1.00}O_{7-\delta}$:CGO (70:30 w%) composite electrodes. The electrode processes are simulated with the circuital models described in the text: $(RQ)_{HF}(RQ)_{IF}(RQ)_{LF}$ in the entire temperature range; (solid black lines represent spectra calculated using the equivalent circuit).

The DRT function at 873 K (Figure 6a) suggests the existence of four electrode processes: one associated to high frequency (2114 Hz), one to intermediate frequency (10 Hz) and two with very similar low relaxation-frequencies (0.3 and 0.8 Hz). These two latter processes could not be simulated with two distinct (RQ) contributions. Therefore, we used a circuital model with three components ($(RQ)_{HF}(RQ)_{IF}(RQ)_{LF}$) to account for the electrode processes

in the temperature range 773 K to 873 K. In addition, a fifth process is apparent at very high frequency, corresponding to oxide diffusion through the grain boundary of the electrolyte pellet. On the other hand, the DRT function at 1073 K (Figure 6b) clearly shows three electrode processes at different frequencies ranges: high (5373Hz), intermediate (185Hz) and low (16Hz). This temperature is high enough the process associated to the electrolyte is no longer observed; in fact, from 923 K this process is not identified in the IS data, nor in the DRT (Figure S5). On heating the maxima decreases and move to higher frequencies suggesting that the three processes are thermally activated,[68] as observed in Figure 7a which shows the thermal evolution of the polarization resistance for each process obtained from the fitting of the IS data.

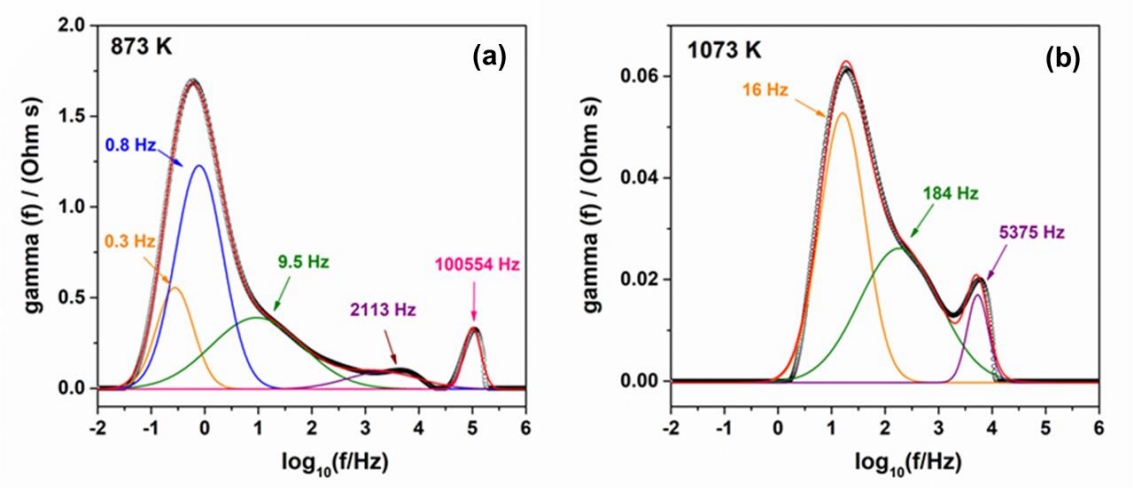

Figure 6. DRTs of IS spectra measured in air for symmetrical cells of composites ESCF1010:CGO (70:30 w%) on CGO at 873 K and 1073 K.

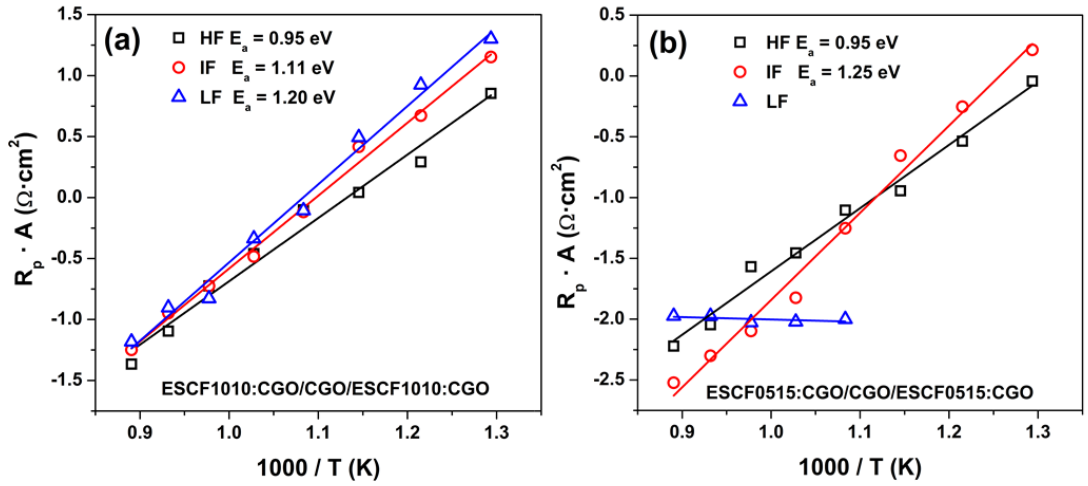

Figure 7. Arrhenius plots of polarization resistance associated to the different processes of the impedance spectra measured in air for symmetrical cells of composites $Eu_2SrCo_xFe_{2-x}O_{7-\delta}$:CGO (70:30 w%) on CGO electrolyte pellets; (a) x = 1.00 and (b) x = 0.5.

The DRT at 873 K corresponding to ESCF0515, (Figure 8a) reveals only two electrode process and the oxide diffusion in the electrolyte pellet.

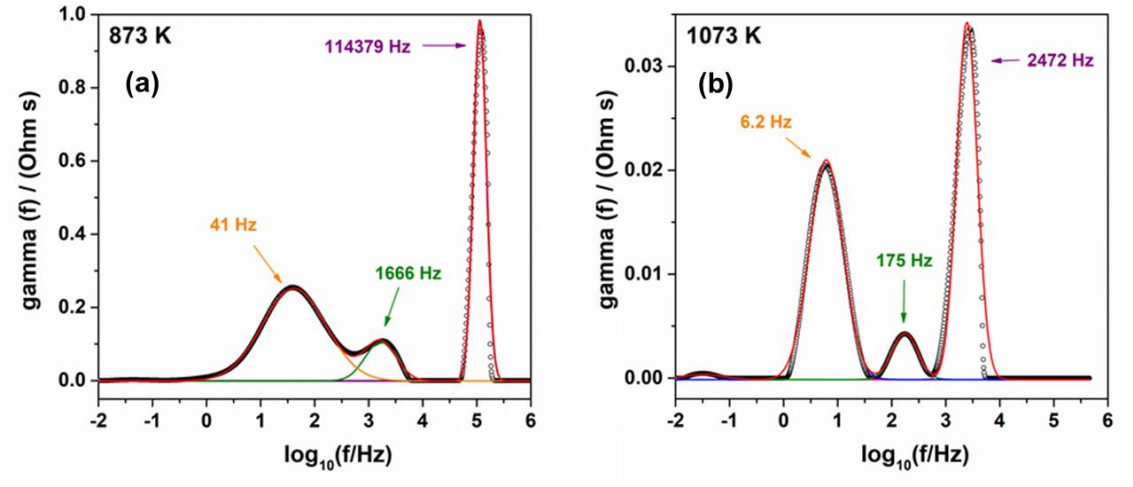

Figure 8. DRTs of IS spectra measured in air for symmetrical cells of composites ESCF0515:CGO (70:30 w%) on CGO at 873 K and 1073 K.

The two electrode processes have relaxation-times corresponding to intermediate frequency (41 Hz) and to high frequency (1666 Hz); oxide diffusion across the electrolyte grain boundaries has a very high characteristic frequency (114379 Hz), like that observed for ESCF1010 in Figure 6a. In the DRT corresponding to 1073 K (Figure 8b) three processes are apparent. All of them correspond to the electrode contribution: at high frequency (2472 Hz), at intermediate frequency (175 Hz) and at low frequencies (6.2 Hz). It seems that an additional process appears at very low frequency (0.06 Hz); however, its physical origin is not clear and one must to recall that DRT function could show extra peaks, with no physical meaning, as was reported earlier.[67] Thus, we disregarded this spurious very weak signal. Therefore, considering DRT results for ESCF0515, we have used the following circuital models: up to 873 K it consists of two series *RQ*-elements whereas from 933 to 1123 K three *RQ*-elements have been considered.

Figure 9 shows the fitting of IS spectra to the corresponding circuital models at different temperatures for ESCF0515. DRT for all the temperatures are plotted in Figure S6. On heating the HF and IF maxima decreases and move to higher frequencies, confirming that these processes are thermally activated,[68] as shown in Figure 8b. However, both the resistance and the characteristic frequency of the LF processes remain unchanged.

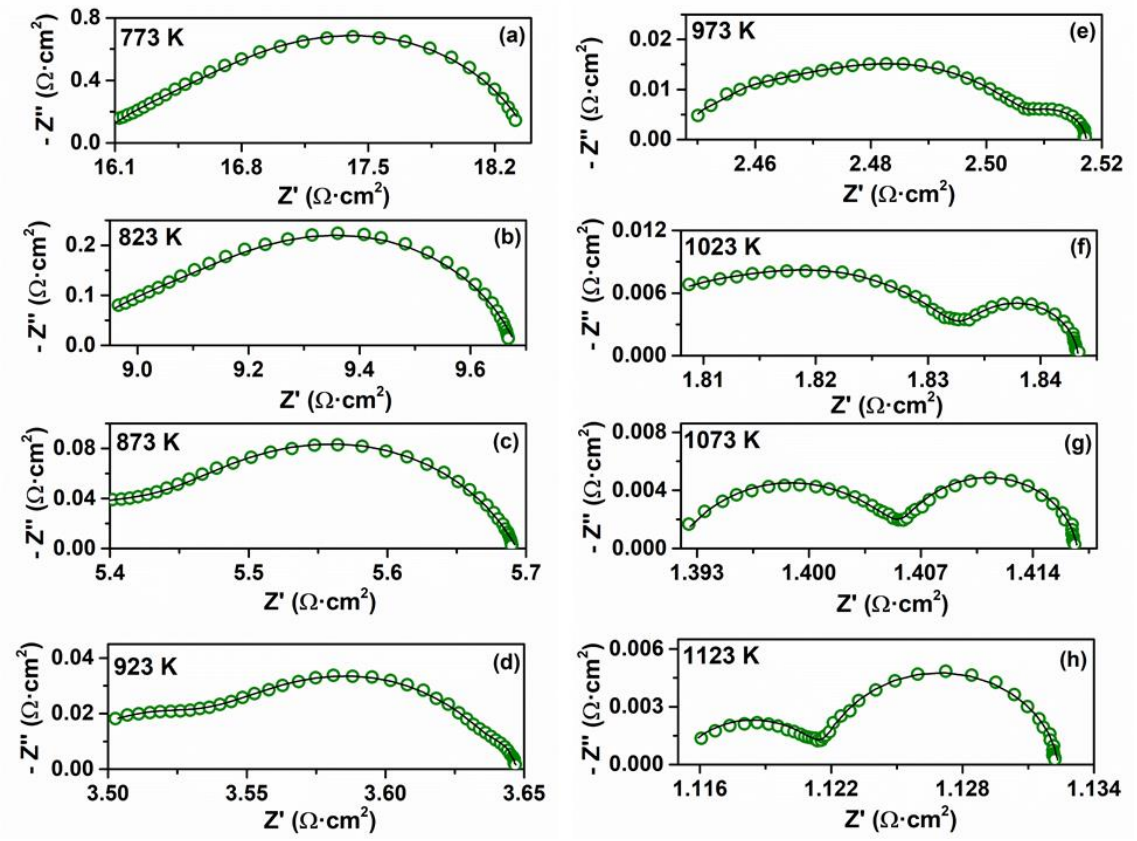

Figure 9. Impedance spectra at operation temperatures from 773 to 1123 K in air on symmetrical cells with $Eu_2SrCo_{0.50}Fe_{1.50}O_{7-\delta}$:CGO (70:30 w%) composite electrodes. The electrode processes are simulated with the circuital models described in the text: $(RQ)_{HF}(RQ)_{IF}$ up to 873 K and $(RQ)_{HF}(RQ)_{IF}(RQ)_{LF}$ from 933 to 1123 K; (solid black lines represent spectra calculated using the equivalent circuits).

To identify the physico-chemical nature of the different processes it is necessary to analyze the parameters associated to them; namely: the characteristic frequency (or the corresponding relaxation-time), the capacitance, the activation energies, etc.

The capacitance and relaxation-frequencies for the HF process obtained from the fitting of the IS spectra are between of 0.001-1000 μFcm^{-2} and 100-0.01 MHz, respectively, for the two samples in the entire temperature range. These values suggest that this process can be assign to oxide-ion transfer through the electrolyte-electrode interface.[51,68,70,71]

In the whole temperature range, for the two samples, the capacitance and relaxation-frequency of the process at intermediate frequencies, are between10^{-2}-10^{-5} Fcm^{-2} and 10^{1}-10^{2} Hz, respectively; this suggests that this process is associated with the electrochemical reaction coupled to charge transfer through the electrode.[68,69,70,71,72]

These kinds of processes are thermally activated, as confirmed in Figure 7. The activation energies of the HF. process for the two materials is identical; however, that of the IF process is higher for the low-cobalt oxide. This may be ascribed to a lower catalytic activity due to lower content of cobalt, which is more active for oxygen reduction than iron.

Finally, the LF process is totally different for ESCF1010 and ESCF0515.

It is well stated that at low frequencies two electrode processes are dominant: oxygen absorption/desorption associated with the reduction/oxidation reaction and diffusion of oxygen gas. For the former the capacitances are in the order of 10^{-2} Fcm^{-2} and the characteristic frequencies in the range 10-100 Hz, whereas in the latter the values are around 1 Fcm^{-2} and 1 Hz, respectively. More importantly, oxygen gas diffusion is not thermally activated being an almost perfect capacitive process, whereas oxygen absorption/desorption associated with the reduction/oxidation reaction is thermally activated.[15.71,73]

For ESCF1010 the LF process is thermally activated (Figure 7) and the characteristic frequencies (Figure S5) and capacitances agree with those corresponding to oxygen absorption/desorption associated with the reduction/oxidation reaction. This contribution is not observed in ESCF0515; the LF process for this material is not thermally activated (Figure 7) and its capacitance and characteristic frequency (Figure S6) values allow to identify this process as oxygen gas diffusion through the electrode pores. The lack of the reduction/oxidation reaction associated with absorption/desorption in the low frequency range in the IS spectra of ESCF0515 at high temperature can be thought as due to its very

low resistance; the compound has a high electronic conductivity and a noticeable concentration of oxygen vacancies which make the process to have a low enough resistance no to appear in the IS spectra.[74] Similar beneficial effect of the combination of high electronic conductivity and high oxygen vacancies concentration has been observed in oxygen reduction in water splitting where the material surface plays a crucial role.[75]

Figure 10 depicts the thermal evolution of the ASR of the electrodes in symmetrical cells for both materials, $Eu_2SrCo_xFe_{2-x}O_{7-\delta}$ (x=0.50 and 1.00). In the entire temperature range, for the low-cobalt containing material, $Eu_2SrCo_{0.50}Fe_{1.50}O_{7-\delta}$, lower values of ASR (around one order of magnitude smaller) are obtained in comparison with the values for $Eu_2SrCo_{1.00}Fe_{1.00}O_{7-\delta}$. ASRs as low as 0.08 $\Omega \cdot cm^2$ and 0.012 $\Omega \cdot cm^2$ were observed in air for ESCF0515 at 973 and 1173 K, respectively; the values increased to 1.15 $\Omega \cdot cm^2$ and 0.1 $\Omega \cdot cm^2$ for ESCF1010 in the same operation conditions. The activation energies for both compounds are close (around 1.1 and 0.9 eV for ESCF1010 and ESCF0515, respectively), suggesting that the limiting cathode process is alike since the thermal dependence is similar. The noticeable difference in the ASR values between the two materials seem to be most likely related with the much higher total conductivity and a high enough concentration of oxygen vacancies at operational conditions for $Eu_2SrCo_{0.50}Fe_{1.50}O_{7-\delta}$ (similar in both oxides), both factors resulting in a superior performance for this low-cobalt material, as observed in other systems.[29] At 973 K in air, the total conductivities are 72.9 $S \cdot cm^{-1}$ for ESCF0515 but only 11.6 $S \cdot cm^{-1}$ for ESCF1010; whereas the concentration of oxygen vacancies are 0.10/7.0 and 0.12/7.0 for ESCF0515 and ESCF1010, respectively. In our previous paper[7] we reported about the properties of the high-cobalt containing member $Eu_2SrCo_{1.50}Fe_{0.50}O_{7-\delta.;}$ In the above conditions this material displays an intermediate ASR (0.26 $\Omega \cdot cm^2$) but the highest total conductivity of the three compounds (83.6 $S \cdot cm^{-1}$) with a high concentration of oxygen

vacancies (0.34/7.00). Good air-electrode SOFC materials should have enough high values of both, electronic and oxide-ionic conductivity, since the electrochemical reaction at the cathode comprises reduction of oxygen gas to ions, and their incorporation and diffusion through the lattice.[74] Therefore, it seems that the oxide $Eu_2SrCo_{0.50}Fe_{1.50}O_{7-\delta}$ presents the best balance between electronic and ionic conductivity, resulting in the best electrochemical performance for this system.

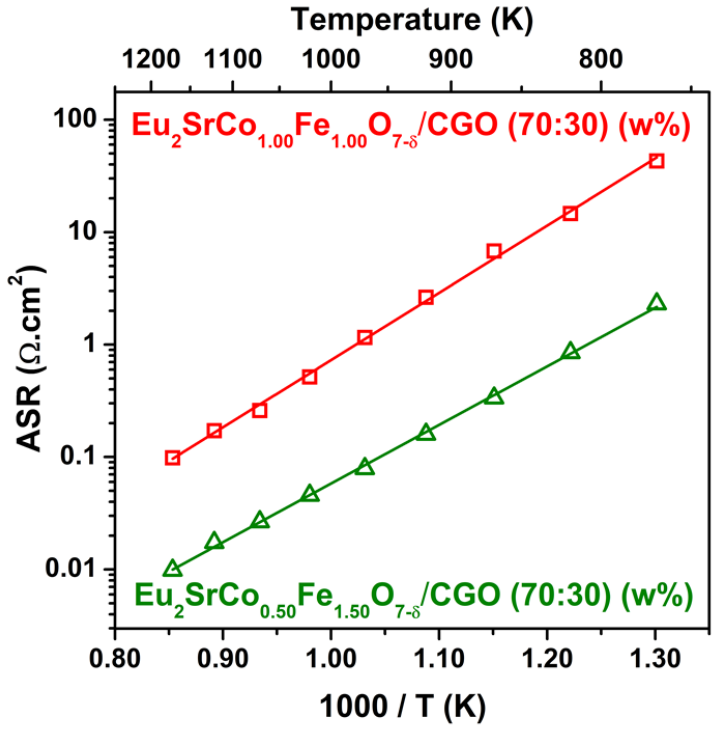

Figure 10. Arrhenius plot of the area–specific resistance (ASR) obtained from the impedance spectra of symmetrical cells with configuration ESCF1010:CGO/CGO/ESCF1010:CGO (red square) and ESCF0515:CGO/CGO/ESCF0515:CGO (green triangle) in air.

Figure S7 shows the cross-sectional views corresponding to electrode/electrolyte interface for the cells made with oxides $Eu_2SrCo_{1.00}Fe_{1.00}O_{7-\delta}$ and $Eu_2SrCo_{1.50}Fe_{0.50}O_{7-\delta}$. The figures

display a general view, revealing the electrodes porosity, which are similar in both cases. Two different kinds of particles with different sizes and morphologies are observed. Particles of the $Eu_2SrCo_xFe_{2-x}O_{7-\delta}$ materials are larger and with regular shape, whereas the much smaller ones are particles of CGO. The thickness of the electrodes is around 30 µm for both samples and good interface contact between the electrolyte and the electrode is observed in both cases.

Conclusions

In this study, we prepared and characterized the $Eu_2SrCo_{1.00}Fe_{1.00}O_{7-\delta}$ and $Eu_2SrCo_{0.50}Fe_{1.50}O_{7-\delta}$ oxides as a novel cathode with low cobalt content for IT-SOFCs.

Both phases are isostructural, as determined by a combination of powder X-ray diffraction with high resolution transmission electron microscopy. A complete cationic ordering of Eu/Sr was obtained since refinements of X-ray data revealed that the two ions occupy different crystallographic A-sites. In addition, tilting of the $(Co/Fe)O_6$ octahedra occurs in the perovskite-like blocks of the Ruddlesden–Popper structure; the tilting angle is larger for larger iron-contents, as the values of the tolerance factors predict.

Both materials are *p-type* semiconductors due to hole-hopping associated to 3d-ions in mixed oxidation states. In $Eu_2SrCo_{1.00}Fe_{1.00}O_{7-\delta}$ the content of Fe is high enough to significantly perturb the low-energy conduction paths involving cobalt; whereas in $Eu_2SrCo_{0.50}Fe_{1.50}O_{7-\delta}$ the movement of holes takes place through adjacent high-energy Fe sites. The concentration of electronic conducting species, associated with Fe^{3+}/Fe^{2+} pairs, is independent of the temperature, in contrast to Co^{3+} that can be reduced easier than Fe^{3+}; thus, at high enough

temperature $Eu_2SrCo_{0.5}Fe_{1.5}O_{7-\delta}$ displays relatively high conductivity via iron in mixed oxidation state.

The TEC value decrease with lower concentration values of Co^{3+} since it limits the associated effect with spin-state transition.

Electrochemical studies on symmetrical cells using the title materials as components of composite cathodes show that the electrodes prepared with $Eu_2SrCo_{0.50}Fe_{1.50}O_{7-\delta}$ exhibit much lower ASR values (0.08 $\Omega \cdot cm^2$ at 973 K in air) than $Eu_2SrCo_{1.00}Fe_{1.00}O_{7-\delta}$ in the same operational conditions (1.15 $\Omega \cdot cm^2$). This decrease may be attributed to the much higher total conductivity and a high enough concentration of oxygen vacancies at operation temperatures, which enhance the activity for oxygen reduction as the balance between electronic and ionic conductivity is optimal. These R-P n=2 oxides show ASR values like the best ones reported so far for other R-P of higher order n=3, such as the series $La_xPr_{4-x}Ni_3O_{10-\delta}$ ($0 \leq x \leq 4$), in similar conditions.[40] In this series the best performance is found for x = 1 ($LaPr_3Ni_3O_{10-\delta}$) with ASR of 0.05 $\Omega \cdot cm^2$ at 1023 K in air; the same value in these conditions is obtained for electrodes of $Eu_2SrCo_{0.50}Fe_{1.50}O_{7-\delta}$. In contrast to what reported in ref. [40], note that in our case no optimization of the electrode microstructure or processing is applied; therefore, even better performances are expected for optimized electrodes made with this material.

The excellent electrochemical performance of the low-cobalt material $Eu_2SrCo_{0.50}Fe_{1.50}O_{7-\delta}$, which show one of the lowest ASR values reported so far for a R-P oxide, makes it a promising candidate for application as an IT-SOFC cathode material in real devices.

Author Information

Corresponding Author*

E-mail: danielmg@icv.csic.es

Fax: (+) (34) 917 355 843

Acknowledgments

We thank "Agencia Estatal de Investigación/Fondo Europeo de Desarrollo Regional" (FEDER/UE) for funding the projects PID2019-106662RB-C41, PID2019-106662RB-C44 and RTI2018-095088-B-I00. We are also grateful to the "Red de Excelencia" (MINECO, MAT 2017-090695-REDT) for facilitating collaboration between the groups. DMG thanks "Ministerio de Ciencia e Innovación" for financial support through a "Juan de la Cierva" grant. UA and MTA also thank USP-CEU for financial support.

ASSOCIATED CONTENT

Supporting Information.

(Figure S1) PXRD patterns of $Eu_2SrCo_xFe_{2-x}O_{7-\delta}$ (x= 1.00 and 0.50) at RT; (Figure S2) LeBail fitting of PXRD patterns of composites with CGO (70:30 w/w) of $Eu_2SrCo_xFe_{2-x}O_{7-\delta}$ (x=1.00 and 0.50); (Figure S3) Relative linear expansion vs temperature and TGA curves in air for $Eu_2SrCo_xFe_{2-x}O_{7-\delta}$ (x= 1.00 and 0.50); (Figure S4) 3d-metal oxidation state variation and oxygen content vs temperature for $Eu_2SrCo_xFe_{2-x}O_{7-\delta}$ (x= 1.00 and 0.50); (Figure S5-S6) DRTs at different temperatures for for $Eu_2SrCo_xFe_{2-x}O_{7-\delta}$ (x= 1.00 and 0.50), respectively; (Figure S7) SEM image of the cross section of symmetrical electrode for $Eu_2SrCo_xFe_{2-x}O_{7-\delta}$ (x= 1.00 and 0.50); (Table S1) Structural parameters for $Eu_2SrCo_xFe_{2-x}O_{7-\delta}$ (x= 1.00 and 0.50); (Table S2) Selected structural information for $Eu_2SrCo_xFe_{2-x}O_{7-\delta}$ (x= 1.00 and 0.50).

References

(1) Aguadero, A.; Alonso, J. A.; Escudero, M. J.; Daza, L. Evaluation of the $La_2Ni_{1-x}Cu_xO_{4+\delta}$ system as SOFC cathode material with 8YSZ and LSGM as electrolytes. *Solid State Ionics* **2008,** 179, 393-400.

(2) Al Daroukh, M.; Vashook, V. V.; Ullmann, H.; Tietz, F.; Arual Raj, I. Oxides of the AMO_3 and A_2MO_4-type: structural stability, electrical conductivity and thermal expansion. *Solid State Ionica* **2003,** 158, 141-150.

(3) Amow, G.; Au, J.; Davidson, I. Synthesis and characterization of $La_4Ni_{3-x}Co_xO_{10\pm\delta}$ ($0.0 \leq x \leq 3.0$, $\Delta x=0.2$) for solid oxide fuel cell cathodes. *Solid State Ionics.* **2006,** 177, 1837-1841.

(4) Amow, G.; Skinner, S. J. Recent developments in Ruddlesden–Popper nickelate systems for solid oxide fuel cell cathodes. *J. Solid State Electr.* **2006,** 10, 538-546.

(5) Boulahya, K.; Hassan, M.; Munoz Gil, D.; Romero, J.; Gomez Herrero, A.; Garcia Martin, S.; Amador, U. Exploring the physical properties of $Eu_2SrCo_{1.5}Mn_{0.5}O_7$, a new n=2 member of the Ruddlesden-Popper series $(Eu,Sr)_{n+1}(Co,Mn)_nO_{3n+1}$ *J. Mater. Chem A* **2015,** 3, 22931-22939.

(6) Boulahya, K.; Munoz Gil, D.; Hassan, M.; Garcia Martin, S.; Amador, U. S Structural and microstructural characterization and properties of new phases in the Nd-Sr-Co-(Fe/Mn)-O system as air-electrodes in SOFCs. *Dalton Trans.* **2017,** 46, 1283-1289.

(7) Boulahya, K.; Muñoz-Gil, D.; Gómez-Herrero, A.; Azcondo, M. T.; Amador, U. $Eu_2SrCo_{1.5}Fe_{0.5}O_7$ a new promising Ruddlesden–Popper member as a cathode component for intermediate temperature solid oxide fuel cells, *J. Mater. Chem. A* **2019,** 7, 5601-5611.

(8) Jennings, A. J.; Skinner, S. J. Thermal stability and conduction properties of the $La_xSr_{2-x}FeO_{4+\delta}$ system. *Solid State Ionics* **2002,** 152, 663-667.

(9) Mazo, G. N.; Kazakov, S. M.; Kolchina, L. M.; Morozov, A. V.; Istomin, S. Y.; Lyskov, N. V.; Gippius, A. A.; Antipov, E. V. Thermal expansion behavior and high-temperature electrical conductivity of $A_{2-x}A_x'Cu_{1-y}Co_yO_{4\pm\delta}$ (A = La, Pr; A' = Pr, Sr) oxides with the K_2NiF_4-type structure. *J. Alloy. Compd.* **2015,** 639, 381-386.

(10) Song, K. W.; Lee, K. T. Characterization of $NdSrCo_{1-x}Fe_xO_{4+\delta}$ ($0 <= x <= 1.0$) intergrowth oxide cathode materials for intermediate temperature solid oxide fuel cells. *Ceram. Int.* **2011,** 37 (2), 573-577.

(11) Wang, J.; Zhou, J.; Yang, J.; Zong, Z.; Fu, L.; Lian, Z.; Zhang, X.; Wang, X.; Chen, C.; Ma, W.; Wu, K. Nanoscale architecture of $(La_{0.6}Sr_{1.4})_{0.95}Mn_{0.9}B_{0.1}O_4$ (B = Co, Ni, Cu) Ruddlesden–Popper oxides as efficient and durable catalysts for symmetrical solid oxide fuel cells. *Renew, Energ.* **2020,** 157, 840-850.

(12) Zhao, H.; Li, Q.; Sun, L. Ln_2MO_4 cathode materials for solid oxide fuel cells. *Sci. China Chem.* **2011,** 54 (6), 898.

(13) Ruddlesden, S. N.; Popper, P. New compounds of the K_2NiF_4 type. *Acta Crystallogr.* **1957,** 10 (8), 538-540.

(14) Ruddlesden, S. N.; Popper, P. The compound $Sr_3Ti_2O_7$ and Its Structure. *Acta Crystallogr.* **1958,** 11, 54-55.

(15) Adler, S. B. Factors governing oxygen reduction in solid oxide fuel cell cathodes. *Chem. Rev.* **2004,** 104, 4791-4843.

(16) Carter, S.; Selcuk, A.; Chater, R. J.; Kajda, J.; Kilner, J. A.; Steele, B. C. H. Oxygen transport in selected nonstoichiometric perovskite-structure oxides. *Solid State Ionics* **1992,** 53-56, 597-605.

(17) Steele, B. C. H. Survey of materials selection for ceramic fuel cells II. Cathodes and anodes. *Solid State Ionics* **1996,** 86-88, 1223-1234.

(18) Tu, H.; Takeda, Y.; Imanishi, N.; Yamamoto, O. $Ln_{1-x}Sr_xCoO_3$(Ln = Sm, Dy) for the electrode of solid oxide fuel cells. *Solid State Ionics* **1997,** 100, 283-288.

(19) Teraoka, Y.; Nobunaga, T.; Okamoto, K.; Miura, N.; Yamazoe, N. Influence of constituent metal cations in substituted $LaCoO_3$ on mixed conductivity and oxygen permeability. *Solid State Ionics* **1991,** 48 (3), 207-212.

(20) Tai, L. W.; Nasrallah, M. M.; Anderson, H. U.; Sparlin, D. M.; Sehlin, S. R. Structure and electrical properties of $La_{1-x}Sr_xCo_{1-y}Fe_yO_3$. Part 2. The system $La_{1-x}Sr_xCo_{0.2}Fe_{0.8}O_3$. *Solid State Ionics* **1995,** 76, 273-283.

(21) Tai, L. W.; Nasrallah, M. M.; Anderson, H. U.; Sparlin, D. M.; Sehlin, S. R. Structure and electrical properties of $La_{1-x}Sr_xCo_{1-y}Fe_yO_3$. Part 1. The system $La_{0.8}Sr_{0.2}Co_{1-y}Fe_yO_3$. *Solid State Ionics* **1995,** 76, 259-271.

(22) Waller, D.; Lane, J. A.; Kilner, J. A.; Steele, B. C. H. The effect of thermal treatment on the resistance of LSCF electrodes on gadolinia doped ceria electrolytes. *Solid State Ionics* **1996,** 86–88, 767-772.

(23) Berenov, A. V.; MacManus-Driscoll, J. L.; Kilner, J. A. Oxygen tracer diffusion in undoped lanthanum manganites. *Solid State Ionics* **1999,** 122 (1), 41-49.

(24) Aguadero, A.; Antonio, J. A.; Pérez-Coll, D.; de La Calle, C.; Fernández-Díaz, M. T.; Goodenough, J. B. $SrCo_{0.95}Sb_{0.05}O_{3-\delta}$ as Cathode Material for High Power Density Solid Oxide Fuel Cells *Chem. Mater.* **2010,** 22, 789-798.

(25) Yang, L.; Zuo, C. D.; Wang, S. Z.; Cheng, Z.; Liu, M. L. A Novel Composite Cathode for Low-Temperature SOFCs Based on Oxide Proton Conductors. *Adv. Mater.* **2008,** 20, 3280-3283.

(26) Serra, J. M.; Vert, V. B. Optimization of Oxygen Activation Fuel-Cell Electrocatalysts by Combinatorial Designs. *ChemSusChem* **2009,** 2, 957-961.

(27) Azcondo, M. T.; Yuste, M.; Pérez-Flores, J. C.; Muñoz-Gil, D.; García-Martín, S.; Muñoz-Noval, A.; Orench, I. P.; García-Alvarado, F.; Amador, U. Defect Chemistry, Electrical Properties, and Evaluation of New Oxides $Sr_2CoNb_{1-x}Ti_xO_{6-\delta}$ ($0 \leq x \leq 1$) as Cathode Materials for Solid Oxide Fuel Cells. *ChemSusChem* **2017,** 10 (14), 2978-2989.

(28) Gómez-Pérez, A.; Azcondo, M. T.; Yuste, M.; Pérez-Flores, J. C.; Bonanos, N.; Porcher, F.; Muñoz-Noval, A.; Hoelzel, M.; García-Alvarado, F.; Amador, U. The A-cation deficient perovskite series $La_{2-x}CoTiO_{6-\delta}$ ($0 \leq x \leq 0.20$): new components for potential SOFC composite cathodes. *J. Mater. Chem A.* **2016**, 4, 3386-3397.

(29) Muñoz-Gil, D.; Azcondo, M. T.; Ritter, C.; Fabelo, O.; Pérez-Coll, D.; Mather, G. C.; Amador, U.; Boulahya, K. T The Effects of Sr Content on the Performance of $Nd_{1-x}Sr_xCoO_{3-\delta}$ Air-Electrode Materials for Intermediate Temperature Solid Oxide Fuel Cells under Operational Conditions. *Inorg. Chem.*, **2020**, 59, 12111-12121.

(30) Efimov, K.; Xu, Q.; Feldhoff, A. Transmission Electron Microscopy Study of $Ba_{0.5}Sr_{0.5}Co_{0.8}Fe_{0.2}O_{3-\delta}$ Perovskite Decomposition at Intermediate Temperatures. *Chem. Mater.* **2010,** 22, 5866-5875.

(31) Shafeie, S.; Grins, J.; Istomin, S. Y.; Gippius, A. A.; Karvonen, L.; Populoh, S.; Weidenkaff, A.; Köhler, J.; Svensson, G. T Tracking of high-temperature thermal expansion and transport properties vs. oxidation state of cobalt between +2 and +3 in the $La_2Co_{1+z}(Ti_{1-x}Mg_x)_{1-z}O_6$-system. *J. Mater. Chem.* **2012,** 22, 16269-16276.

(32) Perez-Flores, J. C.; Gomez-Perez, A.; Yuste, M.; Canales-Vazquez, J.; Climent-Pascual, E.; Ritter, C.; Azcondo, M. T.; Amador, U.; Garcia-Alvarado, F. Characterization

of $La_{2-x}Sr_xCoTiO_6$ ($0.6 \leq x \leq 1.0$) series as new cathodes of solid oxide fuel cells. *Int. J. Hydrog. Energy* **2014,** 39, 5440-5450.

(33) Petric, A.; Huang, P.; Tietz, F. Evaluation of La–Sr–Co–Fe–O perovskites for solid oxide fuel cells and gas separation membranes. *Solid State Ionics* **2000,** 135, 719-725.

(34) Kharton, V. V.; Figueiredo, F. M.; Kovalevsky, A. V.; Viskup, A. P.; Naumovich, E. N.; Yaremchenko, A. A.; Bashmakov, I. A.; Marques, F. M. B. Processing, microstructure and properties of $LaCoO_{3-\delta}$ ceramics, *J. Eur. Ceram. Soc.* **2001,** 21 (13), 2301-2309.

(35) Lee, K. T.; Bierschenk, D. M.; Manthiram, A. $Sr_{3-x}La_xFe_{2-y}Co_yO_{7-\delta}$ ($0.3 \leq x \leq 0.6$ and $0 \leq y \leq 0.6$) intergrowth oxide cathodes for intermediate temperature solid oxide fuel cells. *J. Electrochem. Soc.* **2006,** 153, A1255-A1260.

(36) Lee, K. T.; Manthiram, A. $LaSr_3Fe_{3-y}Co_yO_{10-\delta}$ ($0 \leq y \leq 1.5$) Intergrowth Oxide Cathodes for Intermediate Temperature Solid Oxide Fuel Cells. *Chem. Mater.* **2006,** 18, 1621-1626.

(37) Woolley, R. J.; Skinner, S. J. Functionally graded composite $La_2NiO_{4+\delta}$ and $La_4Ni_3O_{10-\delta}$ solid oxide fuel cell cathodes. *Solid State Ionics* **2014,** 255, 1-5.

(38) Amow, G.; Davidson, I. J.; Skinner, S. J. A comparative study of the Ruddlesden-Popper series, $La_{n+1}Ni_nO_{3n+1}$ (n=1, 2 and 3), for solid-oxide fuel-cell cathode applications. *Solid State Ionics* **2006,** 177, 1205-1210.

(39) Berger, C.; Bucher, E.; Egger, A.; Schrödl, N.; Lammer, J.; Gspan, C.; Merkle, R.; Grogger, W.; Maier, J.; Sitte, W. Oxygen surface exchange kinetics and electronic conductivity of the third-order Ruddlesden-Popper phase $Pr_4Ni_{2.7}Co_{0.3}O_{10-\delta}$. *Solid State Ionics* **2020,** 348, 115282-115291.

(40) Yatoo, M. A.; Du, Z.; Yang, Z.; Zhao, H.; Skinner, S. J. $La_xPr_{4-x}Ni_3O_{10-\delta}$: Mixed A-Site Cation Higher-Order Ruddlesden-Popper Phase Materials as Intermediate-Temperature Solid Oxide Fuel Cell Cathodes. *Crystals* **2020,** 10 (6), 428-541.

(41) Huan, Y.; Chen, S.; Zeng, R.; Wei, T.; Dong, D.; Hu, X.; Huang, Y. Intrinsic Effects of Ruddlesden-Popper-Based Bifunctional Catalysts for High-Temperature Oxygen Reduction and Evolution. *Adv. Energy Mater.* **2019,** 9, 1901573.

(42) Huan, D.; Shi, N.; Zhang, L.; Tan, W.; Xie, Y.; Wang, W.; Xia, C.; Peng, R.; Lu, Y. New, Efficient, and Reliable Air Electrode Material for Proton-Conducting Reversible Solid Oxide Cells. *ACS Appl. Mater. Inter.* **2018,** 10, 1761-1770.

(43) Zhao, Y.; Zhang, K.; Wei, Z.; Li, Z.; Wang, Y.; Zhu, Z.; Liu, T. Performance and distribution of relaxation times analysis of Ruddlesden-Popper oxide $Sr_3Fe_{1.3}Co_{0.2}Mo_{0.5}O_{7-\delta}$ as a potential cathode for protonic solid oxide fuel cells. *Electrochim. Acta.* **2020,** 352, 136444-136455.

(44) Wang, Q.; Hou, J.; Fan, Y.; Xi, X.-a.; Li, J.; Lu, Y.; Huo, G.; Shao, L.; Fu, X.-Z.; Luo, J.-L. $Pr_2BaNiMnO_{7-\delta}$ double-layered Ruddlesden–Popper perovskite oxides as efficient cathode electrocatalysts for low temperature proton conducting solid oxide fuel cells, *J. Mater. Chem A.* **2020,** 8 (16), 7704-7712.

(45) El Shinawi, H.; Greaves, C. ynthesis and characterization of the K_2NiF4 phases $La_{1+x}Sr_{1-x}Co_{0.5}Fe_{0.5}O_{4-\delta}$ (x = 0, 0.2), *J. Solid State Chem.* **2008,** 181 (10), 2705-2712.

(46) Jin, C.; Liu, J. Preparation of $Ba_{1.2}Sr_{0.8}CoO_{4+\delta}$delta K_2NiF_4-type structure oxide and cathodic behavioral of $Ba_{1.2}Sr_{0.8}CoO_{4+\delta}$-GDC composite cathode for intermediate temperature solid oxide fuel cells. *J. Alloy. Compd.* **2009,** 474 (1-2), 573-577.

(47) Skinner, S. J.; Kilner, J. A. Oxygen diffusion and surface exchange in $La_{2-x}Sr_xNiO_{4+\delta}$. *Solid State Ionics* **2000,** 135, 709-712.

(48) Rodríguez-Carvajal, J. Recent advances in magnetic structure determination by neutron powder diffraction. *Phys.B* **1993,** 192, 55-69.

(49) Yuste, M.; Perez-Flores, J. C.; de Paz, J. R.; Azcondo, M. T.; Garcia-Alvarado, F.; Amador, U. New perovskite materials of the $La_{2-x}Sr_xCoTiO_6$ series. *Dalton Trans.* **2011,** 40, 7908-7915.

(50) Johnson, D. *ZView: A software Program for IES Analysis* **2005,** (Scribner Associates, Inc.).

(51) Adler, S. B. Mechanism and kinetics of oxygen reduction on porous $La_{1-x}Sr_xCoO_{3-\delta}$ electrodes. *Solid State Ionics* **1998,** 111 (1-2), 125-134.

(52) Gurusinghe, N. N. M.; de la Figuera, J.; Marco, J. F.; Thomas, M. F.; Berry, F. J.; Greaves, C. Synthesis and characterisation of the n=2 Ruddlesden-Popper phases $Ln_2Sr(Ba)Fe_2O_7$ (Ln = La, Nd, Eu). *Mater. Res. Bull.* **2013,** 48 (9), 3537-3544.

(53) Harrison, W. T. A.; Hegwood, S. L.; Jacobson, A. J. A powder neutron diffraction determination of the structure of $Sr_6Co_5O_{15}$, formerly described as the low-temperature hexagonal form of $SrCoO_{3-x}$. *J. Chem. Soc. Chem. Comm.* **1995**, 1953-1954.

(54) Boulahya, K.; Parras, M.; Gonzalez-Calbet, J. M. Structural chemistry of an n=1 member of the Ruddlesden-Popper $Sr_{n+1}(Co_{0.5}Ta_{0.5})_nO_{3n+1}$ homologous series: Sr_4CoTaO_8. *Eur. J. Inorg. Chem.* **2007,** 14, 2068-2071.

(55) Boulahya, K.; Parras, M.; Gonzalez-Calbet, J. M. Strategies to stabilize new oxides in the $Sr_{n+1}(CoTa)_nO_{3n+1}$ Ruddlesden-Popper homologous series. *Chem.-Eur. J.* **2007,** 13, 910-915.

(56) Battle, P. D.; Green, M. A.; Laskey, N. S.; Millburn, J. E.; Murphy, L.; Rosseinsky, M. J.; Sullivan, S. P.; Vente, J. F. Layered Ruddlesden-Popper manganese oxides: Synthesis and cation ordering. *Chem. Mater.* **1997,** 9, 552-559.

(57) Shannon, R. Revised effective ionic radii and systematic studies of interatomic distances in halides and chalcogenides. *Acta Crystallogr. A* **1976,** 32, 751-767.

(58) Glazer, A. The classification of tilted octahedra in perovskites. *Acta Crystallogr. B* **1972,** 28, 3384-3392.

(59) Munoz-Gil, D.; Perez-Coll, D.; Urones-Garrote, E.; Amador, U.; Garcia-Martin, S. Influence of the synthesis conditions on the crystal structure and properties of $GdBaCo_{2-x}Fe_xO_{5+\delta}$ oxides as air-electrodes for intermediate temperature solid oxide fuel cells. *J. Mater. Chem A* **2017,** 5, 12550-12556.

(60) Aguadero, A.; Perez-Coll, D.; Alonso, J. A.; Skinner, S. J.; Kilner, J. A New Family of Mo-Doped $SrCoO_{3-\delta}$ Perovskites for Application in Reversible Solid State Electrochemical Cells. *Chem. Mater* **2012,** 24, 2655-2663.

(61) Munoz-Gil, D.; Urones-Garrote, E.; Perez-Coll, D.; Amador, U.; Garcia-Martin, S. Crystal structure and compositional effects on the electrical and electrochemical properties of $GdBaCo_{2-x}Mn_xO_{5+\delta}$ ($0 \leq x \leq 2$) oxides for use as air electrodes in solid oxide fuel cells, *J. Mater. Chem A* **2018,** 6 (13), 5452-5460.

(62) Maupoey, Z.; Azcondo, M. T.; Amador, U.; Kuhn, A.; Perez-Flores, J. C.; de Paz, J. R.; Bonanos, N.; Garcia-Alvarado, F. The role of the Eu^{3+}/Eu^{2+} redox-pair in the electrical properties of $Sr_2EuNb_{1-x}Ti_xO_{6-\delta}$ oxides, *J. Mater. Chem* **2012,** 22, 18033-18042.

(63) Volkova, N. E.; Gavrilova, L. Y.; Cherepanov, V. A.; Aksenova, T. V.; Kolotygin, V. A.; Kharton, V. V. Synthesis, crystal structure and properties of $SmBaCo_{2-x}Fe_xO_{5+\delta}$. *J. Solid State Chem.* **2013,** 204, 219-223.

(64) Lee, K. T.; Manthiram, A. Synthesis and characterization of $Nd_{0.6}Sr_{0.4}Co_{1-y}Mn_yO_{3-\delta}$ ($0 \leq y \leq 1.0$) cathodes for intermediate temperature solid oxide fuel cells. *J. Power Sources* **2006,** 158, 1202-1208.

(65) Kirkpatrick, S. Percolation and Conduction. *Rev. Mod. Phys.* **1973,** 45 (4), 574-588.

(66) Kaczmarczyk, J.; Zasada, F.; Janas, J.; Indyka, P.; Piskorz, W.; Kotarba, A.; Sojka, Z. Thermodynamic Stability, Redox Properties, and Reactivity of Mn_3O_4, Fe_3O_4, and Co_3O_4 Model Catalysts for N_2O Decomposition: Resolving the Origins of Steady Turnover. *ACS Catal.* **2016,** 6, 1235-1246.

(67) Ivers-Tiffée, E.; Weber, A. Evaluation of electrochemical impedance spectra by the distribution of relaxation times. *J. Ceram. Soc. Jpn.* **2017**, 125, 193-201.

(68) Costamagna, P.; Sala, E. M.; Zhang, W.; Lund Traulsen, M.; Holtappels, P. Electrochemical impedance spectroscopy of $La_{0.6}Sr_{0.4}Co_{0.2}Fe_{0.8}O_{3-\delta}$ nanofiber cathodes for intermediate temperature-solid oxide fuel cell applications: A case study for the 'depressed' or 'fractal' Gerischer element. *Electrochim. Acta* **2019,** 319, 657-671.

(69) Escudero, M.J.; Aguadero, A.; Alonso, J.A.; Daza, L., A kinetic study of oxygen reduction reaction on La_2NiO_4 cathodes by means of impedance spectroscopy, *J. Electroanal. Chem.* **2007**, 611, 107-116.

(70) Azcondo, M.T.; Yuste, M.; Pérez-Flores, J.C.; Muñoz-Gil, D.; García-Martín, S.; Muñoz-Noval, A.; Orench, I.; García-Alvarado, F.; Amador, U. Defect Chemistry, Electrical Properties, and Evaluation of New Oxides $Sr_2CoNb_{1-x}Ti_xO_{6-\delta}$ ($0 \leq x \leq 1$) as Cathode Materials for Solid Oxide Fuel Cells *ChemSusChem* **2017**, 10, 2978.

(71) Ortiz-Vitoriano, N.; Hauch, A.; Ruiz de Larramendi, I.; Bernuy-López, C.; Knibbe, R.; Rojo, T. Electrochemical characterization of $La_{0.6}Ca_{0.4}Fe_{0.8}Ni_{0.2}O_{3-\delta}$ perovskite cathode for IT-SOFC *J. Power Sources*, **2013**, 239,196-200.

(72) Nielsen, J.; Jacobsen, T.; Wandel, M. mpedance of porous IT-SOFC LSCF:CGO composite cathodes. *Electrochim. Acta* **2011,** 56, 7963-7974.

(73) Flura, A.; Nicollet, C.; Fourcade, S.; Vibhu, V.; Rougier, A.; Bassat, J. M.; Grenier, J. C. Identification and modelling of the oxygen gas diffusion impedance in SOFC porous electrodes: application to $Pr_2NiO_{4+\delta}$, *Electrochim. Acta* **2015,** 174, 1030-1040.

(74) Merkle, R.; Maier, J. How is oxygen incorporated into oxides? A comprehensive kinetic study of a simple solid-state reaction with $SrTiO_3$ as a model material. *Angew. Chem. Int. Edit.***2008,** 47 (21), 3874-3894.

(75) Grimaud, A.; Diaz-Morales, O.; Han, B.; Hong, W.T.; Lee, Y-L; Giordano, L.; Stoerzinger, K.A.; Koper, M.; Saho-Horn, Y, Activating lattice oxygen redox reactions in metal oxides to catalyse oxygen evolution. *Nature Chem.* **2017**, 9, 457–465.

For Table of Contents Only

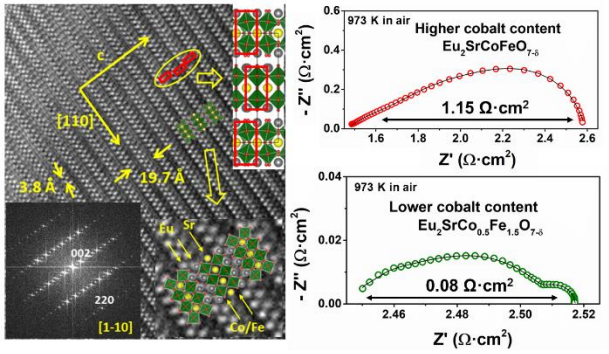

Synopsis: The n=2 member of the Ruddlesden–Popper system $(Eu,Sr)_{n+1}(Co,Fe)_nO_{3n+1}$, $Eu_2SrCo_{0.50}Fe_{1.50}O_{7-\delta}$ with low cobalt content, shows excellent electrochemical performance as a cathode material in Solid Oxide Fuel Cells at intermediate-temperature. This is related with its high total conductivity and sufficient concentration of oxygen vacancies at operation temperatures, producing an optimal balance between electronic and ionic conductivity.